Excitons in planar quantum wells based on transition metal dichalcogenides

Pavel V. Ratnikov*

A.M. Prokhorov General Physics Institute, Russian Academy of Sciences, ul. Vavilova 38, 119991 Moscow, Russia

(Received 30 April 2020; revised 22 July 2020; accepted 24 July 2020; published 10 August 2020)

The problem of a size quantization for charge carriers in a planar quantum well consisting of different monolayers of transition metal dichalcogenides is solved using the Dirac model and the four-band model. For excitons, bound states of electrons and holes at the size quantization levels in such a quantum well, the energy spectrum was found in two cases: the Bohr radius is much smaller than the width of the quantum well (dielectric permeability of a substrate is relatively small) and the Bohr radius is much larger than it (the case of a strong dielectric screening). It is shown that the energy spectra in these two cases are completely different. A method for the synthesis of the heterostructures under consideration is also proposed.

DOI: 10.1103/PhysRevB.102.085303

I. INTRODUCTION

The solid-state physics community is fascinated by two-dimensional (2D) materials. Great interest is caused by their unusual properties and the prospects provided by them in many areas, from nanoelectronics and photovoltaics to biological applications (e.g., biosensors or drug delivery). One of the brightest representatives of this rich diverse cohort is graphene, the most well-studied-to-date 2D crystal.

Since the 2010s, different 2D materials have been used as the "design cubes" of vertical (layered) heterostructures. Transition metal dichalcogenides (TMDs) and their doped versions are particularly noteworthy for this purpose. Individual layers of 2D materials may be stacked on each other to synthesize single and double quantum wells (QWs), superlattices, etc. The layers are bound together through van der Waals attraction. Therefore, such heterostructures are also referred to as *van der Waals heterostructures* [1].

Given the number of different ways for stacking 2D materials, it is possible to manufacture van der Waals heterostructures with any required properties. The inclusion of thin TMD layers in these heterostructures allows one to observe many-particle effects in systems with long-lifetime charge carriers. At low temperatures, they may exhibit a superfluidity of excitons and superconductivity due to coupling of spatially separated quasiparticles [2–12] and condensation into an electron-hole liquid [13–17]. Indirect excitons in van der Waals TMD-based heterostructures are recently studied in Ref. [18].

TMDs have a general chemical formula MX_2 with a transition metal atom M usually from groups IV–VII (e.g., Hf, Nb, Ta, Mo, W, or Re) and two chalcogen atoms X (S, Se, or Te). Their crystal structure was first established by Linus Pauling in 1923 [19]. The monomolecular layer (monolayer) of TMD is a three-layer sandwich with a layer of metal atoms M inserted between two layers of chalcogen atoms X. Atoms in each layer are packed in a triangular lattice. Depending on the relative position of these layers, several types of structural phases are distinguished, mainly trigonal prismatic (2H) or octahedral (1T) phases. The 2H phases correspond to an ABA stacking when chalcogen atoms from different layers are located above each other. The 1T phases have an ABC stacking order. The thermodynamically stable phase is either the 2H or 1T phase. There also are the orthorhombic (distorted octahedral) $1T_d$ and the monoclinic $1T'$ phases, which are often metastable ones [20]. For example, WTe_2 is undergoing the structure phase transition $1T_d \rightarrow 1T'$ at high pressure [21,22]. The structure and synthesis of TMDs are described in more detail in Ref. [23].

By the end of the 1960s, about 60 TMDs were investigated, more than two-thirds of which had a layered structure [24]. Most of them are semiconductors with an indirect band gap of $\sim$1 eV. The qualitative change occurs when going over from the bulk sample to the monolayer. It turned out that many 2D TMDs, including such well-known representatives as MoS_2, $MoSe_2$, WS_2, and WSe_2, become direct-band semiconductors with a band gap of about 2 eV [25–27].

Monolayers of TMDs have the conduction and valence-band extrema at the corners of the 2D hexagonal Brillouin zone [28,29]. Similar to graphene, there are two inequivalent valleys for low-energy carriers. Since their intervalley scattering is suppressed, belonging to one of the two valleys (the valley index) may be considered a "good" quantum number. The usage of the valley degree of freedom in TMDs yields a promising option for nanoelectronics with the valley-selective charge carriers transport, called valleytronics. This is made possible by the valley-selective excitation of charge carriers with a circularly polarized electromagnetic wave [30–33].

We propose here a planar one-dimensional (1D) quantum well structure based on TMDs (Sec. II). This paper is mainly devoted to two issues: the size quantization of charge carriers in such QWs (Sec. III) and the energy spectrum of excitons in them depending on the dielectric environment (Sec. IV). These very straightforward questions are nevertheless very important for the physics of planar heterostructures composed

*ratnikov@lpi.ru

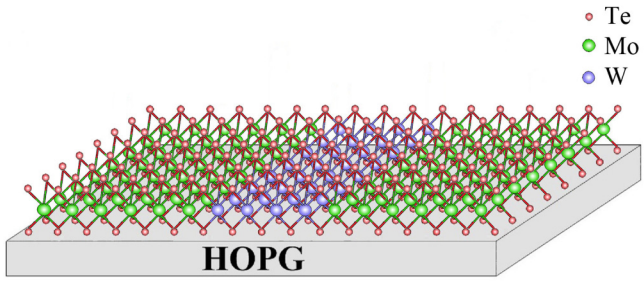

FIG. 1. Schematic representation of the proposed here $MoTe_2/WTe_2/MoTe_2$ planar QW. Highly ordered pyrolytic graphite (HOPG) is used as a substrate.

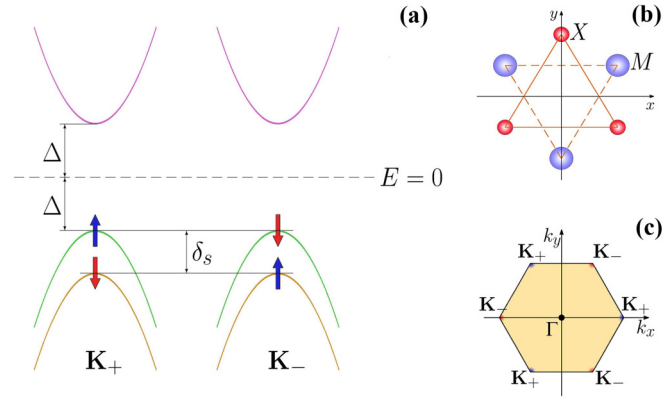

FIG. 2. (a) The lower conduction band and the upper valence band at two valleys $\mathbf{K}_+$ and $\mathbf{K}_-$. The spin splitting of the conduction band is neglected, considering it as spin degenerate, while the valence band has a strong spin splitting. (b) A top view of one section of a TMD crystal lattice with a coordinate reference (in the case of the heterostructure under consideration M = Mo, W and X = Te). (c) The Brillouin zone of TMDs in the form of a regular hexagon with $\mathbf{K}_+$ and $\mathbf{K}_-$ points in the corners.

of 2D materials. The planar heterostructures proposed in this paper have not yet been grown. However, other similar systems have been obtained. In our opinion, both isolated nanoribbons of 2D materials and their sets are of interest due to their quasi-1D geometry and monomolecular thickness. These systems are briefly discussed in Sec. IV C. In Sec. V, we discuss the possibilities to manufacture the TMD-based QWs [34] and summarize our results.

II. MONOLAYER PLANAR QUANTUM WELL BASED ON TMDS

We propose here a type of TMD-based planar heterostructures, namely, $MoSe_2/WTe_2/MoSe_2$ or $MoTe_2/WTe_2/MoTe_2$ single QWs. A schematic representation of the latter is given in Fig. 1.

Both QWs are examples of type-I QWs owing to the ratio of the band-gap E_g and electron affinity χ for monolayer of $MoSe_2$ ($E_g = 2.25$ eV [35] and $\chi = 3.21$ eV) [36], WTe_2 ($E_g = 1.18$ eV [37] and $\chi = 3.69$ eV [38]), and $MoTe_2$ ($E_g = 1.72$ eV [39] and $\chi = 3.4$ eV [40]).

Such QWs can be synthesized as a result of varying transition metal atoms in one plane. Although this is a rather complex approach, it brings a greater challenge from the technological side, which may push for further progress in the field of heterostructure synthesis.

In what follows, we investigate theoretically the electron and hole size quantization and confined excitons in the proposed TMD-based planar QWs.

III. SIZE QUANTIZATION PROBLEM FOR CHARGE CARRIERS

A. Dirac model

The Dirac model is very constructive from the methodological side, allowing us to obtain a rather simple dispersion relation for the size quantization levels. However, it is insufficient to describe the asymmetry of the dispersion of electrons and holes in the **K** valleys, since it automatically gives equal effective masses for them. This model does not take into account the absence of the center of inversion in the material. Considering these circumstances is necessary, for example, when analyzing the splittings of the spin levels of excitons in a magnetic field. The Dirac model leads to the same g factors of the conduction band and the valence band, which, in turn, determines the absence of splittings of the spin levels of excitons in a magnetic field. However, the available experimental data show the presence of such splittings [41].

These features can be taken into account by including in the effective Hamiltonian the nearest in energy bands of the same parity, the bands $c + 2$ and $v - 3$ [42]. Such a four-band Hamiltonian is presented in Sec. III B.

We emphasize that from the point of view of performing computations (numerical calculations), the Dirac model is also useful as the first iteration to find the size quantization levels. This makes it easier to find the right solutions within the four-band model.

Often, in the Dirac model for TMDs, the lower valence band split by spin-orbit interaction is also taken into account. The effective Hamiltonian has the corresponding term, which is proportional to the spin operator $\widehat{s}_z$ [30]. Here, we write the Hamiltonian as [43]

$$\widehat{H} = \gamma_3 \boldsymbol{\sigma} \widehat{\mathbf{p}}^{\tau} + \Delta\sigma_z + \left(\tau s_z - \frac{1}{2}\right)\delta_s \frac{1-\sigma_z}{2}, \qquad (1)$$

where γ_3 is the band parameter, similar to Fermi velocity v_F in graphene, $\widehat{\mathbf{p}}^{\tau} = (\tau\widehat{p}_x, \widehat{p}_y)$, $\widehat{p}_x = -i\partial_x$, and $\widehat{p}_y = -i\partial_y$ are components of the momentum operator ($\hbar = 1$), $\tau = \pm 1$ is the valley index ($\tau = +1$ for the valley $\mathbf{K}_+$ and $\tau = -1$ for the valley $\mathbf{K}_-$, see Figs. 2(a) and 2(c), $\Delta = E_g/2$ is the half width of the band gap between the lower conduction band (c) and the upper valence band (v). The matrices σ_x, σ_y, and σ_z are the Pauli matrices. The quantum number $s_z = \pm\frac{1}{2}$ is the eigenvalue of the spin operator $\widehat{s}_z$. The quantity δ_s is spin splitting at the valence band top caused by the spin-orbit interaction.

According to the results of first-principles calculations based on density-functional theory, there are giant spin splittings from $\delta_s = 148$ meV for MoS_2 to $\delta_s = 456$ meV for WSe_2 [44] and $\delta_s = 480$ meV for WTe_2 [45].

In our opinion, such a large splitting allows us to omit the last term in Eq. (1) in the framework of the two-band model and consider only the two nearest bands, namely, spin-polarized valence band with spin $\uparrow$ for $\tau = +1$ and spin $\downarrow$ for $\tau = -1$. Thus, we arrive at the 2×2 effective Dirac Hamiltonian,

$$\widehat{H}_{\mathrm{D}}^{\tau} = \gamma_3 \boldsymbol{\sigma} \widehat{\mathbf{p}}^{\tau} + \Delta \sigma_z + V, \tag{2}$$

where the scalar potential V describes the possible displacement of the middle of the band gap relative to the vacuum level E_{vac} when we compare different TMDs.

The 2×2 Dirac equation is

$$\widehat{H}_{\mathrm{D}}^{\tau} \Psi_{\tau} = E_{\tau} \Psi_{\tau}, \quad \Psi_{\tau} = \begin{pmatrix} \psi_{\tau}^{c} \\ \psi_{\tau}^{v} \end{pmatrix}, \tag{3}$$

where the scalar envelope wave functions ψ_{τ}^{c} and ψ_{τ}^{v} describe states in the conduction band and the valence band, respectively. Such a description can be constructed by analogy with the description of states on two mutually penetrating triangular Bravais sublattices A and B of graphene. For the TMD crystal lattice of the 2H phase, we can also see two mutually penetrating triangular sublattices in layers of X and M atoms in a top view [see Fig. 2(b)]. The valley index τ is written in the general case at energy as well. As will be shown below, asymmetry between valleys is present in an asymmetric QW, due to the explicit dependence of the energy of charge carriers on τ. Note that there is no such dependence for symmetric QWs.

The 4×4 Dirac Hamiltonian Eq. (2) is similar to the Dirac Hamiltonian in quantum electrodynamics (QED) $\widehat{H}_{\mathrm{D}} = c\boldsymbol{\alpha}\widehat{\mathbf{p}} + \beta\Delta + V$, where $\boldsymbol{\alpha} = \left(\begin{smallmatrix} O & \sigma \\ \sigma & O \end{smallmatrix}\right)$ and $\beta = \left(\begin{smallmatrix} I & O \\ O & -I \end{smallmatrix}\right)$ are the Dirac matrices (O and I are the zero and unit matrices, respectively). Four-vector of the current density in QED is $j_{\mu} = (\overline{\Psi}\gamma_0\Psi,\ c\overline{\Psi}\boldsymbol{\gamma}\Psi)$, where $\overline{\Psi} = \Psi^{\dagger}\gamma_0$ is the Dirac conjugate bispinor and $\gamma_0 = \beta$ and $\boldsymbol{\gamma} = \gamma_0\boldsymbol{\alpha} = \left(\begin{smallmatrix} O & \sigma \\ -\sigma & O \end{smallmatrix}\right)$ are the Dirac γ matrices in the standard representation. It is seen that $\widehat{H}_{\mathrm{D}}$ transfers to $\widehat{H}_{\mathrm{D}}^{\tau}$ after replacements $c \to \gamma_3$, $\boldsymbol{\alpha} \to \boldsymbol{\sigma}$, $\beta \to \sigma_z$, and $\widehat{\mathbf{p}} \to \widehat{\mathbf{p}}^{\tau}$ with a decrease in the dimensionality of the space from 3 to 2. Therefore, when we repeat the output of the expression for the current density operator as in QED, we get that the "current density" is expressed by $\mathbf{j}^{\tau} = \gamma_3 \Psi_{\tau}^{\dagger} \boldsymbol{\sigma} \Psi_{\tau}$. The components of this vector $j_x^{\tau} = \gamma_3(\psi_{\tau}^{c*}\psi_{\tau}^{v} + \psi_{\tau}^{v*}\psi_{\tau}^{c})$ and $j_y^{\tau} = -i\gamma_3(\psi_{\tau}^{c*}\psi_{\tau}^{v} - \psi_{\tau}^{v*}\psi_{\tau}^{c})$ must be continuous when passing through the boundary between two materials, $j_x^{\tau}|_L = j_x^{\tau}|_R$ and $j_y^{\tau}|_L = j_y^{\tau}|_R$, i.e., $\gamma_3\psi_{\tau}^{c*}\psi_{\tau}^{v}|_L = \gamma_3\psi_{\tau}^{c*}\psi_{\tau}^{v}|_R$. Here, the indexes L and R denote belonging to the region to the left and to the right of the boundary, respectively. The last equality is ensured by performing equalities $\sqrt{\gamma_3}\psi_{\tau}^{c}|_L = \sqrt{\gamma_3}\psi_{\tau}^{c}|_R$ and $\sqrt{\gamma_3}\psi_{\tau}^{v}|_L = \sqrt{\gamma_3}\psi_{\tau}^{v}|_R$ or the equality

$$\sqrt{\gamma_3}\Psi_{\tau}|_L = \sqrt{\gamma_3}\Psi_{\tau}|_R. \tag{4}$$

The boundary condition Eq. (4) is also established for Ψ_{τ} by integrating the Dirac Eq. (3) in the vicinity of the interface between the media [46,47].

Now, let us consider a QW. In the general case, we consider an asymmetric QW (e.g., $MoTe_2/WTe_2/MoSe_2$). Each region is characterized by numbers γ_{3i}, Δ_i, and V_i ($i = 1, 2, 3$). Its energy diagram is shown schematically in Fig. 3. The $E = 0$ level is set to coincide with the middle of the band gap in the

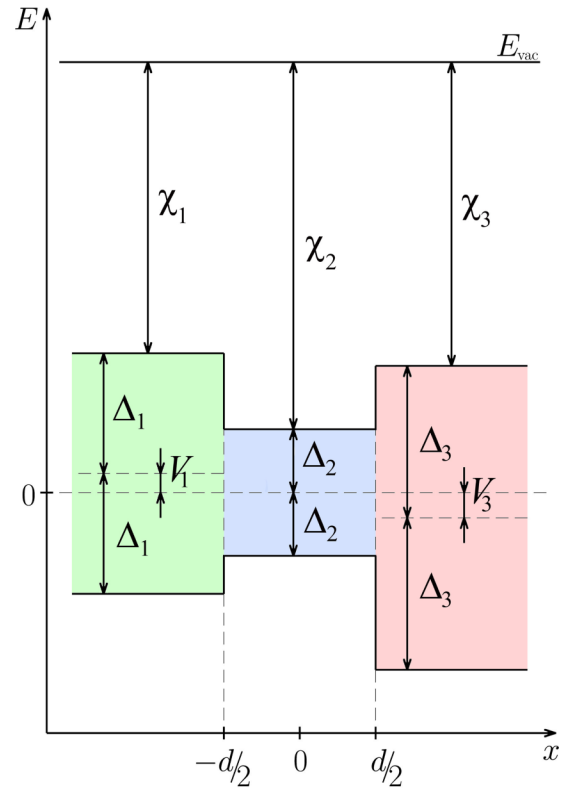

FIG. 3. The energy diagram for QW under analysis: E_{vac} is the vacuum level and χ_i ($i = 1, 2, 3$) is the electron affinity.

QW region, a strip of the TMD with a smaller band gap, so $V_2 = 0$. Then, the values of the scalar potential for the barrier regions are

$$\begin{aligned} V_1 &= \Delta_2 + \chi_2 - (\Delta_1 + \chi_1), \\ V_3 &= \Delta_2 + \chi_2 - (\Delta_3 + \chi_3), \end{aligned} \tag{5}$$

where χ_i is the electron affinity, i.e., a distance in energy of the edge of the conduction band to the vacuum level E_{vac} (see also Fig. 2).

The x axis is directed perpendicular to the QW interfaces (the orientation of the axes is shown in Fig. 2(b)). The width of the QW is d. We consider the boundaries between the materials as sharp. The solution to the Dirac Eq. (3) in three regions is

(1) $x < -d/2$

$$\Psi_{\tau 1} = C_1 \begin{pmatrix} 1 \\ \varkappa_{\tau 1} \end{pmatrix} e^{k_1 x + i k_y y}, \tag{6}$$

$$\varkappa_{\tau 1} = \frac{i\gamma_{31}(-\tau k_1 + k_y)}{E_{\tau} + \Delta_1 - V_1} \text{ and } E_{\tau} = V_1 \pm \sqrt{\Delta_1^2 + \gamma_{31}^2(k_y^2 - k_1^2)};$$

(2) $-d/2 < x < d/2$

$$\Psi_{\tau 2} = C_2 \begin{pmatrix} 1 \\ \varkappa_{\tau 2}^{+} \end{pmatrix} e^{i(k_2 x + k_y y)} + \widetilde{C}_2 \begin{pmatrix} 1 \\ \varkappa_{\tau 2}^{-} \end{pmatrix} e^{i(-k_2 x + k_y y)}, \tag{7}$$

$$\varkappa_{\tau 2}^{\pm} = \frac{\gamma_{32}(\pm\tau k_2 + i k_y)}{E_{\tau} + \Delta_2} \text{ and } E_{\tau} = \pm\sqrt{\Delta_2^2 + \gamma_{32}^2\left(k_y^2 + k_2^2\right)};$$

(3) $x > d/2$

$$\Psi_{\tau 3} = C_3 \begin{pmatrix} 1 \\ \varkappa_{\tau 3} \end{pmatrix} e^{-k_3 x + i k_y y}, \tag{8}$$

$\varkappa_{\tau 3} = \frac{i\gamma_{33}(\tau k_3 + k_y)}{E_\tau + \Delta_3 - V_3}$ and $E_\tau = V_3 \pm \sqrt{\Delta_3^2 + \gamma_{33}^2\left(k_y^2 - k_3^2\right)}$.

Pluses and minuses in Eqs. (6)–(8) the expression for the energy E_τ correspond to electrons and holes, respectively. The constants C_1, C_2, $\widetilde{C}_2$, and C_3 are found from the boundary condition Eq. (4) and the normalization condition for wave functions Eqs. (6)–(8):

$$\int_{-\infty}^{\infty} \Psi_\tau^\dagger \Psi_\tau dx = 1. \tag{9}$$

Using also the boundary condition Eq. (4), we obtain that the carrier energy spectrum is determined by the following dispersion relation:

$$\tan(k_2 d) = \frac{\tau A_\tau^- \gamma_{32} k_2}{A_\tau^+ \gamma_{32} k_y - B_\tau (E_\tau + \Delta_2) - C_\tau (E_\tau - \Delta_2)}, \tag{10}$$

where

$$\begin{aligned} A_\tau^\pm &= \gamma_{31}(-\tau k_1 + k_y)(E_\tau + \Delta_3 + V_3) \\ &\pm \gamma_{33}(\tau k_3 + k_y)(E_\tau + \Delta_1 + V_1), \\ B_\tau &= \gamma_{31}\gamma_{33}(-\tau k_1 + k_y)(\tau k_3 + k_y), \\ C_\tau &= (E_\tau + \Delta_1 + V_1)(E_\tau + \Delta_3 + V_3). \end{aligned}$$

Due to the explicit dependence on τ in Eq. (10), the dispersion curve in one valley does not coincide with the dispersion curve in another valley, but they turn into each other when the sign of k_y is changed. The valleys are connected via the time inversion transformation.

For the symmetric QW when $\gamma_{33} = \gamma_{31}$, $\Delta_3 = \Delta_1$, and $V_3 = V_1$ [the potential barrier on the right is the same as on the left and the system is symmetric with respect to the $x \to -x$ transformation], the explicit dependence on τ disappears and Eq. (10) is rewritten as

$$\tan(k_2 d) = \frac{\gamma_{31}\gamma_{32} k_1 k_2}{E(E - V_1) - \Delta_1\Delta_2 - \gamma_{31}^2 k_y^2}.$$

B. Four-band model

As stated in the beginning of Sec. III A, the transition to the four-band model is carried out by adding bands of the same parity as the lower conduction band c and the upper valence band v, and lying in energy in proximity to them: Above c there is $c+2$, below v there is $v-3$ [41].

Let us work in the basis of wave functions $\{|\psi_\tau^{c+2}\rangle, |\psi_\tau^c\rangle, |\psi_\tau^v\rangle, |\psi_\tau^{v-3}\rangle\}$. The effective Hamiltonian 4×4 has the form [48]

$$\widehat{H}_{4\mathrm{b}}^\tau = \begin{pmatrix} E_{c+2} & \gamma_6 \widehat{p}_-^\tau & \gamma_4 \widehat{p}_+^\tau & 0 \\ \gamma_6 \widehat{p}_+^\tau & E_c & \gamma_3 \widehat{p}_-^\tau & \gamma_5 \widehat{p}_+^\tau \\ \gamma_4 \widehat{p}_-^\tau & \gamma_3 \widehat{p}_+^\tau & E_v & \gamma_2 \widehat{p}_-^\tau \\ 0 & \gamma_5 \widehat{p}_-^\tau & \gamma_2 \widehat{p}_+^\tau & E_{v-3} \end{pmatrix}. \tag{11}$$

Here, $\widehat{p}_\pm^\tau = \tau \widehat{p}_x \pm i\widehat{p}_y$ and γ_2, γ_3, γ_4, γ_5, and γ_6 are the band parameters. The band edges E_{v-3}, E_v, E_c, and E_{c+2} are counted from the middle of the band gap between c and v bands. For reasons of conformity with the Dirac model, we take $E_v = -\Delta_i + V_i$ and $E_c = \Delta_i + V_i$. Moreover, it is possible to put $V_2 = 0$ for QW region.

We also consider the boundaries between materials to be sharp, so smooth potentials do not arise in the boundary regions, and the band parameters γ_j ($j = 2-6$) are constants in each medium up to the boundary. Therefore, the "symmetrization" of the Hamiltonian Eq. (11) by the introduction of anticommutators $\gamma_j \widehat{p}_\pm^\tau \to \frac{1}{2}\{\gamma_j, \widehat{p}_\pm^\tau\}$ is not required so it remains Hermitian [46].

The equation for the four-component envelope wave function with Hamiltonian Eq. (11),

$$\widehat{H}_{4\mathrm{b}}^\tau \Psi_\tau = E_\tau \Psi_\tau, \tag{12}$$

gives for free charge carriers the dispersion relation $\det(H_{4\mathrm{b}}^\tau - E_\tau) = 0$ [$H_{4\mathrm{b}}^\tau$ with $\widehat{p}_\pm^\tau \to k_\pm^\tau = \tau k_x \pm i k_y$] which is the equation on E_τ of the fourth power in quasimomentum $\mathbf{k}$:

$$\begin{aligned} &(E_{c+2} - E_\tau)(E_c - E_\tau)(E_v - E_\tau)(E_{v-3} - E_\tau) - (E_v - E_\tau)(E_{v-3} - E_\tau)\gamma_6^2 k_+^\tau k_-^\tau \\ &- (E_{c+2} - E_\tau)(E_{v-3} - E_\tau)\gamma_3^2 k_+^\tau k_-^\tau - (E_c - E_\tau)(E_{v-3} - E_\tau)\gamma_4^2 k_+^\tau k_-^\tau - (E_{c+2} - E_\tau)(E_c - E_\tau)\gamma_2^2 k_+^\tau k_-^\tau \\ &- (E_{c+2} - E_\tau)(E_v - E_\tau)\gamma_5^2 k_+^\tau k_-^\tau + (E_{v-3} - E_\tau)\gamma_3\gamma_4\gamma_6 (k_+^\tau)^3 + (E_{c+2} - E_\tau)\gamma_2\gamma_3\gamma_5 (k_+^\tau)^3 \\ &+ (E_{v-3} - E_\tau)\gamma_3\gamma_4\gamma_6 (k_-^\tau)^3 + (E_{c+2} - E_\tau)\gamma_2\gamma_3\gamma_5 (k_-^\tau)^3 + (\gamma_2\gamma_6 - \gamma_4\gamma_5)^2 (k_+^\tau k_-^\tau)^2 = 0. \end{aligned} \tag{13}$$

In the quadratic in momentum approximation for electrons $E_\tau \approx E_c + \frac{k_+^\tau k_-^\tau}{2m_c^*}$ and for holes $E_\tau \approx E_v - \frac{k_+^\tau k_-^\tau}{2m_v^*}$, we obtain from Eq. (13) the expressions for the effective mass of electrons m_c^* and holes m_v^* [48]

$$\begin{aligned} \frac{1}{m_c^*} &= 2\left[\frac{\gamma_5^2}{E_c - E_{v-3}} + \frac{\gamma_3^2}{E_c - E_v} + \frac{\gamma_6^2}{E_c - E_{c+2}}\right], \\ \frac{1}{m_v^*} &= 2\left[\frac{\gamma_5^2}{E_{v-3} - E_v} + \frac{\gamma_3^2}{E_c - E_v} + \frac{\gamma_6^2}{E_{c+2} - E_v}\right]. \end{aligned} \tag{14}$$

It can be seen that $m_v^* \neq m_c^*$.

Eliminating the wave function components ψ_τ^{c+2} and ψ_τ^{v-3} in Eq. (12), we arrive at an effective Hamiltonian that takes into account the influence of the $c+2$ and $v-3$ bands,

$$\widehat{H}^\tau = \widehat{H}_{\rm D}^\tau + \delta\widehat{H}^\tau, \tag{15}$$

where

$$\delta\widehat{H}^\tau = \begin{pmatrix} A_{56}\widehat{p}_+^\tau\widehat{p}_- & B_{46}^{25}\widehat{p}_+^\tau\widehat{p}_+^\tau \\ B_{46}^{25}\widehat{p}_-^\tau\widehat{p}_-^\tau & A_{24}\widehat{p}_+^\tau\widehat{p}_-^\tau \end{pmatrix},$$

$$A_{ij} = \frac{\gamma_i^2}{E_\tau - E_{v-3}} - \frac{\gamma_j^2}{E_{c+2} - E_\tau}\ (i=2,\ 5;\ j=4,\ 6),$$

$$B_{46}^{25} = \frac{\gamma_2\gamma_5}{E_\tau - E_{v-3}} - \frac{\gamma_4\gamma_6}{E_{c+2} - E_\tau}.$$

In the quadratic in momentum approximation, the equation $\widehat{H}^\tau\Psi_\tau = E_\tau\Psi_\tau$ with the Hamiltonian Eq. (15) for the wave function $\Psi_\tau = \begin{pmatrix}\psi_\tau^c \\ \psi_\tau^v\end{pmatrix}$ can be reduced to two equations separately for the functions $\psi_\tau^{c,v}$:

$$\left(\frac{1}{2m_{c,v}^*}\widehat{p}_+^\tau\widehat{p}_-^\tau + E_{c,v}\right)\psi_\tau^{c,v} = E_\tau\psi_\tau^{c,v}. \tag{16}$$

The effective masses are given by Eqs. (14).

Equations (16) are second-order differential equations, so additional boundary conditions are needed that are different from Eq. (4). They must ensure, as in the case of the usual Hamiltonian in the Schrödinger equation, the continuity of the current density through the boundary between two materials for electrons $j_x^e = \frac{-i}{2m_c^*}(\psi^{c*}\partial_x\psi^c - \psi^c\partial_x\psi^{c*})$ and for holes $j_x^h = \frac{-i}{2m_v^*}(\psi^{v*}\partial_x\psi^v - \psi^v\partial_x\psi^{v*})$. This is achieved with the continuity of ψ_τ^c and ψ_τ^v and combinations $m_c^{*-1}\partial_x\psi_\tau^c$ and $m_v^{*-1}\partial_x\psi_\tau^v$, which is analogous to the boundary condition used in Ref. [49] and generalized by Bastard [50,51].

Thus, we can solve the QW size quantization problem for electrons with the wave function ψ_τ^c and for holes with the wave function ψ_τ^v, satisfying Eq. (17), using the following boundary conditions:

$$\psi_\tau^{c,v}\big|_L = \psi_\tau^{c,v}\big|_R,\quad \frac{1}{m_{c,v}^*}\partial_x\psi_\tau^{c,v}\bigg|_L = \frac{1}{m_{c,v}^*}\partial_x\psi_\tau^{c,v}\bigg|_R. \tag{17}$$

It should be noted that the valley index τ disappears from Eq. (17): $\widehat{p}_+^\tau\widehat{p}_-^\tau \equiv \widehat{p}_x^2 + \widehat{p}_y^2$ ($\tau^2 = 1$). Thus, the four-band model reduced to Eq. (16) does not take into account possible valley asymmetry of dispersion curves corresponding to size quantization levels, but the electron-hole asymmetry is clearly taken into account. This is more important for finding the exciton energy spectrum. In what follows, we omit the τ index of wave functions and energy.

Now, let us get the dispersion relation for the size quantization levels in the QW. For definiteness, let us consider the case of electrons and characterize each region of QW by numbers E_{ci} and m_{ci}^* ($i=1,\ 2,\ 3$) [for holes, the energy sign changes and $c \to v$]. The solution of Eq. (16) in three regions is

(1) $x < -d/2$

$$\psi^c = c_1 e^{k_1 x + ik_y y}, \tag{18a}$$

$$E = E_{c1} + \frac{1}{2m_{c1}^*}\left(k_y^2 - k_1^2\right), \tag{18′}$$

(2) $-d/2 < x < d/2$

$$\psi^c = c_2 e^{i(k_2 x + k_y y)} + \widetilde{c}_2 e^{i(-k_2 x + k_y y)}, \tag{19a}$$

$$E = E_{c2} + \frac{1}{2m_{c2}^*}\left(k_y^2 + k_2^2\right), \tag{19′}$$

(3) $x > d/2$

$$\psi^c = c_3 e^{-k_3 x + ik_y y}, \tag{20a}$$

$$E = E_{c3} + \frac{1}{2m_{c3}^*}\left(k_y^2 - k_3^2\right). \tag{20′}$$

The constants c_1, c_2, $\widetilde{c}_2$, and c_3 are found from the normalization condition for wave functions Eqs. (18a)–(20a), similar to Eq. (9). Matching the wave functions at the QW boundaries $x = -d/2$ and $x = d/2$, we obtain the dispersion relation for electrons on the size quantization levels:

$$\tan(k_2 d) = k_2\frac{m_{c1}^* k_3 + m_{c3}^* k_1}{\widetilde{m}_c^* k_2^2 - m_{c2}^* k_1 k_3},\ \widetilde{m}_c^* \equiv \frac{m_{c1}^* m_{c3}^*}{m_{c2}^*}. \tag{21}$$

Eliminating k_1 and k_3 from Eq. (21) using Eqs. (18′)–(20′), we can find the function $k_2(k_y)$ and, consequently, the energy $E_{N_e}(k_y)$ for each N_eth size quantization level according to Eq. (19′). Since the valley asymmetry is absent, the extremum of all dispersion curves $E_{N_e}(k_y)$ lies at $k_y = 0$, i.e., at $\mathbf{K}_+$ or $\mathbf{K}_-$ point in the Brillouin zone. The first derivative of the function $k_2(k_y)$ at the point $k_y = 0$ is equal to zero, $k_{20}' = k_2'(k_y = 0) = 0$. The same is true for holes. The effective mass of electrons on the N_eth size quantization level is given by

$$\frac{1}{m_c^*} = \frac{\partial^2 E_{N_e}}{\partial k_y^2}\bigg|_{k_y=0} = \frac{1 + k_{20}k_{20}''}{m_{c2}^*}, \tag{22}$$

where $k_{20} = k_2(k_y = 0)$ and $k_{20}'' = k_2''(k_y = 0)$ are values of the function $k_2(k_y)$ and its second derivative at the point $k_y = 0$.

For a symmetric QW [$E_{c3} = E_{c1}$ and $m_{c3}^* = m_{c1}^*$], Eq. (21) is reduced to

$$\tan(k_2 d) = \frac{k_1 k_2}{\kappa k_2^2 - m_{c2}^* U_0},\ \kappa \equiv \frac{m_{c1}^* + m_{c2}^*}{2m_{c2}^*}, \tag{21′}$$

where $U_0 = E_{c1} - E_{c2}$ is the height of potential barriers. Equation (21′) is equivalent to Eq. (3) in the solution of problem 2 after Sec. 22 of Ref. [52], when the effective masses m_{c1}^* and m_{c2}^* are the same and $\kappa = 1$.

As an example, let us calculate the size quantization levels in $MoTe_2/WTe_2/MoTe_2$ QW with the values of parameters E_{ci} and E_{vi} obtained from the ratio of the band gaps E_{gi} and the electron affinity χ_i ($i=1$ for $MoTe_2$, $i=2$ for WTe_2) presented in Sec. II. The height of potential barriers for electrons is $U_0^e = \chi_2 - \chi_1 = 290$ meV and for holes is $U_0^h = \chi_1 + E_{g1} - (\chi_2 + E_{g2}) = 250$ meV. The effective masses of electrons and holes are $m_{c1}^* = 0.655m_0$, $m_{c2}^* = 0.246m_0$ and $m_{v1}^* = 0.618m_0$, $m_{v2}^* = 0.3m_0$ (m_0 is the free electron mass) [45]. The QW width d is taken as a multiple of the lattice constant b (the distance between neighboring tellurium atoms in one layer), $b = 3.52$ Å [53]. We take $d = 15b = 5.28$ nm. Using Eq. (21′) for electrons and its analog for holes, we determine three electron levels and three hole levels inside the QW [$E_{N_e}^e - E_{c2} < U_0^e$ and $E_{v2} - E_{N_h}^h < U_0^h$] [see Fig. 4(a)]. Using the formula Eq. (22) for the electron effective mass

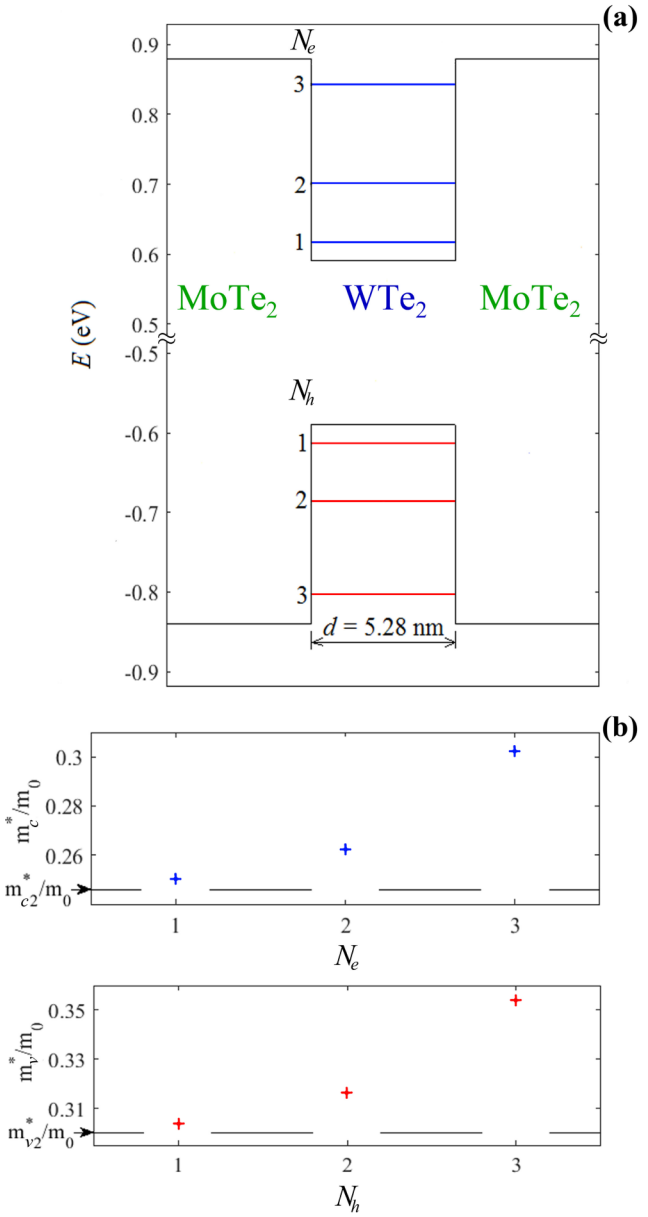

FIG. 4. The results of numerical calculations for the $MoTe_2/WTe_2/MoTe_2$ heterostructure. (a) Values of the energy for size quantization levels of electrons ($E_1^e = 616.5$ meV, $E_2^e = 700.8$ meV, $E_3^e = 842.8$ meV) and of holes ($E_1^h = -613.6$ meV, $E_2^h = -685.9$ meV, $E_3^h = -803.4$ meV). (b) Values of the effective mass of electrons ($m_c^*/m_0 = 0.25, 0.262, 0.302$) [the upper panel] and of holes ($m_v^*/m_0 = 0.304, 0.316, 0.354$) [the lower panel] at the extremes of the corresponding dispersion curves.

and its analog for holes, we find the corresponding effective masses. Note that with an increase in the size quantization level number, the effective mass increases for both electrons and holes [see Fig. 4(b)].

Similarly, one can find size quantization levels and the corresponding effective masses in the potential well for holes in the valence band split off by spin-orbit interaction. For this, one should substitute the effective hole masses m_{v1}^* and m_{v2}^* of the split-off valence band into an equation similar to Eq. (21′).

IV. EXCITONS

A striking feature of the excitons in monolayers of TMDs is their large binding energy and small Bohr radius in the ground state (the $1s$ state). Typical values are $|E_{1s}| \simeq 500$ meV and $a_1 \simeq 10$ Å for freely suspended films in vacuum [41].

Two series of peaks are often observed in the photoluminescence spectrum of TMD monolayers due to a large spin splitting of the valence band, usually named A and B. Peak A corresponds to the exciton which is the binding state of an electron in the conduction band c and a hole in the upper valence band v, while peak B corresponds to the exciton with a hole in the valence band split off by the magnitude of the spin splitting δ_s [see Fig. 1(a)]. The peak B has a blue shift relative to the peak A.

The additional advantage of WTe_2 in the QW region is the largest valence band spin splitting among the TMD monolayers, $\delta_s = 480$ meV [45]. Thus, the energy distance between peaks A and B will also be the largest in $MoTe_2/WTe_2/MoTe_2$ QW. Moreover, $\delta_s > U_0^{e,h}$. This makes it possible to excite only the A peak when the frequency interval of the exciting laser $\omega_{\min} < \omega < \omega_{\max}$ is chosen so $\omega_{\max} - \omega_{\min} < \delta_s$ and $E_g(WTe_2) < \omega_{\max} < E_g(MoTe_2)$, e.g., $\omega_{\min} = E_1^e - E_1^h$ and $\omega_{\max} = E_3^e - E_3^h$ for the example considered at the end of Sec. II. Below, we focus only on the A exciton energy spectrum. Although it will become clear from the foregoing that the calculation of the B exciton energy spectrum is completely analogous if an effective mass of holes is found in the band split off by the spin.

We consider the planar QW as the monolayer film system on the substrate. The Bohr radius of exciton a_1 will always be greater than its value for a suspended film. However, unlike large samples of the TMD monolayers, we have an additional characteristic scale of distances in QW, its width d. Therefore, two cases should be distinguished: (i) a weak dielectric screening when $a_1 \ll d$ (e.g., in the case of the SiO_2 substrate) and (ii) a strong dielectric screening when $a_1 \gg d$ (e.g., in the case of the TiO_2 substrate).

A. Weak dielectric screening

The above presented typical values of the binding energy $|E_{1s}|$ and of the Bohr radius a_1 support the applicability of a description of the exciton in the TMD films by the smooth envelope functions method, when the exciton wave function covers a large number of crystal unit cells [41].

Since the "size" of the excitons is assumed to be much smaller than the width of the QW, the motion of the electron and hole will be quasi-2D in the WTe_2 stripe, neglecting the charge carrier motion along the z axis.

The Hamiltonian describing the 2D relative electron-hole motion in the exciton is

$$\widehat{H}_{\rm ex} = \widehat{T} + \widehat{U}, \tag{23}$$

$$\widehat{T} = \frac{1}{2\mu^*}\left(\frac{\partial^2}{\partial\rho^2} + \frac{1}{\rho}\frac{\partial}{\partial\rho} - \frac{l^2}{\rho^2}\right), \tag{24}$$

$$\widehat{U} = -\frac{\pi\tilde{e}^2}{2r_0'}\left[H_0\left(\frac{\rho}{r_0'}\right) - Y_0\left(\frac{\rho}{r_0'}\right)\right]. \tag{25}$$

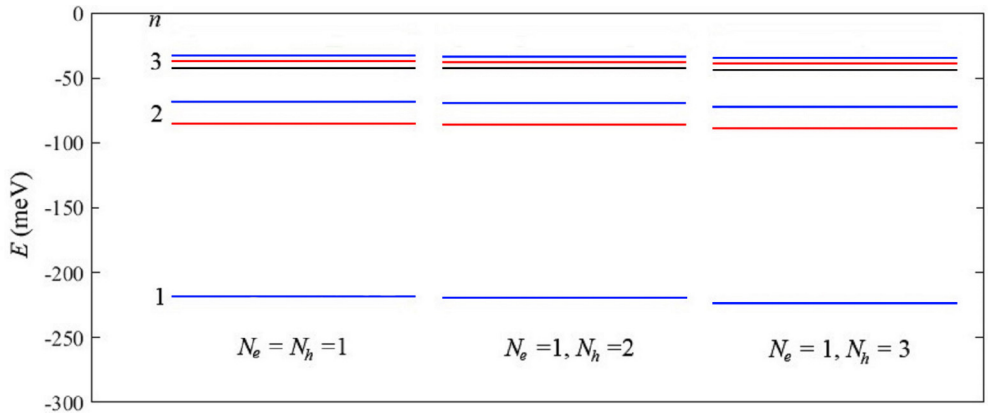

FIG. 5. Three groups of levels for three excitons in the QW $MoTe_2/WTe_2/MoTe_2$ on the silicon dioxide substrate: for the exciton formed by the electron and the hole with $N_e = N_h = 1$ (left), with $N_e = 1$ and $N_h = 2$ (center), and with $N_e = 1$ and $N_h = 3$ (right). The s levels ($l = 0$) are marked in blue, the p levels ($l = 1$) are red, and the d levels ($l = 2$) are black.

Here, μ^* is the reduced mass of the electron and hole, $\mu^{*-1} = m_c^{*-1} + m_v^{*-1}$, and $\rho = |\boldsymbol{\rho}_e - \boldsymbol{\rho}_h|$ is the distance between the electron and hole in the plane $z = 0$, $\boldsymbol{\rho}_{e,h} = (x_{e,h}, y_{e,h}, 0)$. The quantum number l is the angular momentum, $l = 0, 1, 2, \ldots$ We introduced the notation $\widetilde{e}^2 = e^2/\varepsilon_{\text{eff}}$, where $\varepsilon_{\text{eff}} = (\varepsilon_1 + \varepsilon_2)/2$ is the effective dielectric constant (ε_1 and ε_2 are values of the dc permittivity of the materials above and below the film, respectively) [54,55]. Quantity $r_0' = r_0/\varepsilon_{\text{eff}}$ and $r_0 = 2\pi\alpha_{2D}$, and α_{2D} is the 2D susceptibility of the QW region material (in our case, this is WTe_2), which can be estimated as $\widetilde{\alpha}_{2D} = L_c(\varepsilon_\perp - 1)/4\pi$ with the interlayer separation between two chalcogen atoms layers L_c and the in-plane component of the dielectric tensor $\varepsilon_\perp$ [56]. As a rule, in comparison with α_{2D}, obtained in calculations using density-functional theory, this estimate is an estimate from above, i.e., $\alpha_{2D} \lesssim \widetilde{\alpha}_{2D}$. The functions H_0 and Y_0 are the Struve function and the Bessel function of the second kind (the Neumann function), respectively. The potential Eq. (25) was derived by Keldysh [55].

To calculate the energy spectrum of the exciton, we use the variational approach. The trial wave function is taken in the form of the eigenfunctions of a 2D hydrogen atom [57],

$$\widetilde{\psi}_{nl}(\rho) = \frac{C_{nl}}{a}\left(\frac{2\rho}{a}\right)^l e^{-\rho/a} L_{n-l-1}^{2l}\left(\frac{2\rho}{a}\right),$$
$$C_{nl} = \sqrt{\frac{(n-l-1)!}{\pi\left(n-\frac{1}{2}\right)(n+l-1)!}}, \tag{26}$$

where $n = 1, 2, \ldots$ is the principal quantum number, $0 \leqslant l \leqslant n-1$, a is the variational parameter, and L_β^α are the associated Laguerre polynomials.

Wave functions Eqs. (26) form a complete orthonormal set

$$\int d^2\rho \widetilde{\psi}_{nl}^*(\rho)\widetilde{\psi}_{n'l'}(\rho) = \delta_{nn'}\delta_{ll'}.$$

When normalizing the wave functions Eqs. (26), we used the expression for the following integral [58]:

$$\int_0^\infty x^{2l+1}e^{-x}\left(L_{n-l-1}^{2l}(x)\right)^2 dx = \frac{(n+l-1)!}{(n-l-1)!}(2n-1).$$

Wave functions Eqs. (26) also qualitatively reproduce the behavior of the exciton wave function obtained by more complex methods, for example, the solution of the Bethe-Salpeter equation (see Figs. 3(b)– 3(e) in Ref. [59]). This confirms the applicability of $\widetilde{\psi}_{nl}(\rho)$ as trial wave functions.

The exciton energy is calculated as the average $\langle n, l|\widehat{H}_{\text{ex}}|n, l\rangle$ for the trial wave functions Eqs. (26) and depends on the variation parameter a:

$$E_{nl}(a) = \langle n, l|\widehat{T}|n, l\rangle + \langle n, l|\widehat{U}|n, l\rangle. \tag{27}$$

It is easy to verify that the average kinetic energy operator Eq. (24) for arbitrary n and l is equal to

$$\langle n, l|\widehat{T}|n, l\rangle = \frac{1}{2\mu^* a^2}. \tag{28}$$

The second term on the right-hand side of Eq. (27) is

$$\langle n, l|\widehat{U}|n, l\rangle = -\frac{(n-l-1)!}{(2n-1)(n+l-1)!}\frac{\pi\widetilde{e}^2}{2r_0'} \times \int_0^\infty x^{2l+1}e^{-x}\left(L_{n-l-1}^{2l}(x)\right)^2 \times [H_0(\varkappa x) - Y_0(\varkappa x)]dx. \tag{29}$$

Hereinafter, $\varkappa = a/2r_0'$.

The equation for the value of a, which corresponds to the minimum of the energy $E_{nl}(a)$, is

$$-\frac{1}{\mu^* a^3} - \frac{(n-l-1)!}{(2n-1)(n+l-1)!}\frac{\pi\widetilde{e}^2}{4r_0'^2} \times \int_0^\infty x^{2(l+1)}e^{-x}\left(L_{n-l-1}^{2l}(x)\right)^2 \times \left[\frac{2}{\pi} - H_1(\varkappa x) + Y_1(\varkappa x)\right]dx = 0 \tag{30}$$

under the condition $\partial^2 E_{nl}(a)/\partial a^2 > 0$.

We calculate the first n from one to three levels of three A excitons formed by the electron and the hole on the size quantization levels $N_e = 1$ and $N_h = 1$, $N_e = 1$ and $N_h = 2$, $N_e = 1$ and $N_h = 3$ (see Fig. 5). We used the estimate $\widetilde{\alpha}_{2D} = L_c(\varepsilon_\perp - 1)/4\pi$ for the 2D susceptibility of WTe_2 with

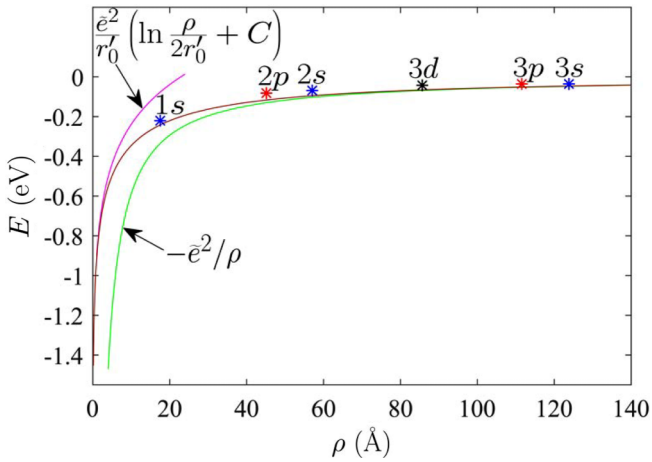

FIG. 6. An illustration of the dependence of E_{nl} on $\langle\rho\rangle_{nl}$ for the first $n = 1 - 3$ levels of the exciton with $N_e = N_h = 1$. The blue stars and the red stars correspond to the ns ($n = 1,\ 2,\ 3$) and np ($n = 2,\ 3$) states, respectively. The black star corresponds to the $3d$ state. Their position in energy is the binding energy in the corresponding state E_{nl}, and their position in the coordinate is determined by the average distance $\langle\rho\rangle_{nl}$ (their numerical values are given in Table I). The brown curve shows potential Eq. (25), which has two asymptotics: at small distances (the magenta curve) and at large distances (the green curve). The constant $C = 0.5772\ldots$ is the Euler constant and $r_0' = 20.39$ Å.

$L_c = c/2 = 7.035$ Å ($c = 14.07$ Å is the size of the unit cell of the bulk sample along the c axis [60]) and $\varepsilon_\perp = 15.2$ [61]. The binding energy of an exciton with increasing N_h slightly increases (all levels shift down in energy) due to an increase in the effective mass of the hole m_v^* and, as a consequence, an increase in the reduced mass μ^*.

Unlike the usual Coulomb potential $-\tilde{e}^2/\rho$, a characteristic feature of the exciton energy spectrum is lifting of degeneracy by the angular momentum l. The levels shift down in energy from the s level with increasing l. With increasing n, the splitting level by l decreases.

It is interesting to note that the exciton levels splitting over l at large n turns out to be small, of the order magnitude of the Coulomb potential change over a large average distance between electron and hole $\langle\rho\rangle_{nl}$. This is illustratively demonstrated in Fig. 6 for the exciton with $N_e = 1$ and $N_h = 1$ (for two other excitons, the picture is qualitatively the same). The energies E_{nl}, values of the variation parameter a, and the average electron-hole distances $\langle\rho\rangle_{nl}$ are presented in the Table I. The average distance $\langle\rho\rangle_{nl}$ calculated with using the trial wave functions Eqs. (26) is proportional to the value of the variational parameter a, which corresponds to the minimum energy $E_{nl}(a)$: $\langle\rho\rangle_{1s} = a$, $\langle\rho\rangle_{2s} = \frac{7}{3}a$, $\langle\rho\rangle_{2p} = 2a$, $\langle\rho\rangle_{3s} = \frac{19}{5}a$, $\langle\rho\rangle_{3p} = \frac{18}{5}a$, $\langle\rho\rangle_{3d} = 3a$ [a is different for each state].

It is worth noting that the $2s$ state has a slightly larger $\langle\rho\rangle_{2s}$ than the QW width d, while the states with $n = 3$ noticeably exceed d (in 1.5 times at least). Nevertheless, we find that the quasi-2D consideration of excitons is applicable in this case, although the $n = 3$ states lie in the intermediate region between the quasi-2D and quasi-1D behavior of excitons.

TABLE I. Calculated values of the energies E_{nl}, of the variation parameter a, and of the average electron-hole distance $\langle\rho\rangle_{nl}$ for the $n = 1 - 3$ states of the exciton with $N_e = N_h = 1$ (the substrate is the SiO_2 plate with $\varepsilon = 3.9$).

State	E_{nl} (meV)	a (Å)	$\langle\rho\rangle_{nl}$ (Å)
$1s$	−217.88	17.67	17.67
$2s$	−68.94	24.41	56.96
$2p$	−85.26	22.48	44.97
$3s$	−32.80	32.62	123.97
$3p$	−37.32	30.99	111.57
$3d$	−42.10	28.56	85.69

Often, starting with $n = 3$, the exciton levels "fall" on the Rydberg series [62], since the potential Eq. (25) approaches the usual Coulomb potential with a good accuracy (both its asymptotics at small and at large distances are also shown in Fig. 6). In the quasi-2D case, the Rydberg series is [41]

$$E_n^{(2D)} = -\frac{\mu^*\tilde{e}^4}{2\left(n-\frac{1}{2}\right)^2}. \tag{31}$$

However, for highly excited states, when $\langle\rho\rangle_{nl} \gg d$, we have the quasi-1D behavior of excitons. As is known, the spectrum of the excited exciton states in this case coincides with the spectrum of a three-dimensional (3D) exciton [63]:

$$E_n^{(1D)} = -\frac{\mu^*\tilde{e}^4}{2n^2}. \tag{32}$$

Therefore, in the intermediate region between the quasi-2D and quasi-1D behavior of excitons, when $\langle\rho\rangle_{nl} \gtrsim d$, the energies E_{nl} lie between the energies Eqs. (31) and (32), $E_n^{(2D)} \lesssim E_{nl} \lesssim E_n^{(1D)}$.

B. Strong dielectric screening

If there is an environment with a large dielectric constant, we obtain that the average electron-hole distance turns out to be much larger than the QW width. Then the behavior of the exciton will be quasi-1D, starting from the ground state. However, the energy of the ground state of an exciton has a logarithmic divergence at short distances in the 1D case [64]. To avoid this divergence in our quasi-1D case, we need to take into account that there is a finite scale across the 1D motion, i.e., the presence of the nonzero QW width d, and enter the cutoff parameter of the Coulomb potential $d_0 \lesssim d$.

On the other hand, the potential Eq. (25) at large distances transforms into the usual Coulomb potential (see also Fig. 6). Therefore, we can solve the 1D Coulomb problem with a potential that depends only on the relative coordinates of the electron and hole along the QW boundaries (here, along the y axis), where the cutoff parameter d_0 is introduced:

$$\widehat{U}^{(1D)} = \begin{cases} -\tilde{e}^2/d_0 & \text{for } |y| < d_0 \\ -\tilde{e}^2/|y| & \text{for } |y| > d_0. \end{cases} \tag{33}$$

The operator of the kinetic energy of the relative 1D motion of the electron and hole is

$$\widehat{T}^{(1D)} = -\frac{1}{2\mu^*}\frac{\partial^2}{\partial y^2}, \tag{34}$$

with the same reduced mass μ^* as above.

As a trial wave function of the ground state, we take

$$\widetilde{\psi}_0(y) = \frac{1}{\sqrt{a_0}} \exp\left(-\frac{|y|}{a_0}\right), \tag{35}$$

where the variational parameter a_0 plays the role of the ground-state Bohr radius.

Averaging Hamiltonian $\widehat{H}_{\rm ex}^{(1D)} = \widehat{T}^{(1D)} + \widehat{U}^{(1D)}$ over the ground-state trial wave function Eq. (35), we express the ground-state exciton energy as [47]

$$E_0 = \frac{1}{2\mu^* a_0^2} - \frac{2\widetilde{e}^2}{a_0} \ln\frac{a_0}{d}. \tag{36}$$

Here, we do not distinguish between d and d_0, since we first carry out the calculation with a logarithmic accuracy.

Minimizing Eq. (36) with respect to a_0, we obtain an equation for a_0:

$$a_0 = \frac{a_1}{2[\ln(a_0/d) - 1]}. \tag{37}$$

To the logarithmic accuracy, $\ln(a_1/d) \gg 1$, we find the relations

$$E_0 = -2\mu^* \widetilde{e}^4 \ln^2(a_1/d), \tag{38}$$

$$a_0 = \frac{a_1}{2\ln(a_1/d)}. \tag{39}$$

When $\ln(a_1/d) \sim 1$, a more accurate variational calculation should be performed using the modified Coulomb potential [47]:

$$\widehat{U}_{\rm m}^{(1D)} = -\frac{\widetilde{e}^2}{\sqrt{y^2 + d_0^2}}. \tag{34'}$$

We average the Hamiltonian with potential $\widehat{U}_{\rm m}^{(1D)}$ over trial function Eq. (35) to obtain

$$E_0 = \frac{1}{2\mu^* a_0^2} - \frac{\pi\widetilde{e}^2}{a_0}\left[H_0\left(\frac{2d_0}{a_0}\right) - Y_0\left(\frac{2d_0}{a_0}\right)\right], \tag{40}$$

where H_0 and Y_0 are the same functions as in Sec. IV A, i.e., the average potential energy in Eq. (40) is given by the value of the potential Eq. (25) at the point $\rho = d_0$ with accuracy to the replacement $r_0' \to a_0/2$.

Minimizing Eq. (40) with respect to a_0, we obtain an equation for a_0:

$$\frac{\pi a_0}{a_1}\left[H_0\left(\frac{2d_0}{a_0}\right) - Y_0\left(\frac{2d_0}{a_0}\right)\right] + \frac{4d_0}{a_1}\left(1 - \frac{\pi}{2}\left[H_1\left(\frac{2d_0}{a_0}\right) - Y_1\left(\frac{2d_0}{a_0}\right)\right]\right) = 1. \tag{41}$$

The numerical value of the parameter d_0 is chosen so the result obtained by solving Eq. (41) coincides with the result Eq. (38) for large $\ln(a_1/d)$.

The energy spectrum of excited states ($n = 1, 2, 3, \ldots$) is given by the formula Eq. (32), and the Bohr radii are $a_n = na_1$ with $a_1 = 1/\mu^*\widetilde{e}^2$ [63].

We also calculated the average electron-hole distances for the ground state and the first three excited states: $\langle|y|\rangle_0 = \frac{1}{2}a_0$, $\langle|y|\rangle_1 = \frac{3}{2}a_1$, $\langle|y|\rangle_2 = 3a_2 = 6a_1$, and $\langle|y|\rangle_3 = \frac{9}{2}a_3 = \frac{27}{2}a_1$.

TABLE II. Calculated values of the energies E_n, of the variation parameter a_n and of the average electron-hole distance $\langle|y|\rangle_n$ for the $n = 0 - 3$ states of the exciton with $N_e = N_h = 1$ (the substrate is the TiO_2 plate with $\varepsilon = 80$).

n	E_n (meV)	a_n (Å)	$\langle\|y\|\rangle_n$ (Å)
0	−3.40	183.33	92.17
1	−1.14	156.10	234.16
2	−0.57	312.21	936.63
3	−0.38	468.31	2107.42

For the ground state, we used the wave function Eq. (35), and for the excited states we took wave functions as eigen wave functions of the Coulomb problem with the potential $-\widetilde{e}^2/|y|$ [47],

$$\psi_n(y) = \frac{\mathrm{sgn}(y)}{\sqrt{2a_n}} \exp\left(-\frac{|y|}{a_n}\right) L_n^{-1}\left(\frac{2|y|}{a_n}\right), \tag{42}$$

where L_n^{-1} are the associated Laguerre polynomials.

The numerical values of the energy E_n, the Bohr radius a_n, and the average electron-hole distance $\langle|y|\rangle_n$ for the $n = 0 - 3$ states of the exciton with $N_e = N_h = 1$ are presented in Table II. The system is placed on the TiO_2 substrate with $\varepsilon = 80$ [65]. The ground state energy was calculated with using of Eq. (41), since $\ln(a_1/d) \approx 1$ [$a_1 = 156.1$ Å and $d = 52.8$ Å]. Here, we took $d_0 = d$.

C. Relation to experimental data

Unfortunately, we did not find modern experimental data regarding the exciton binding energy in heterostructures proposed in this paper. However, the TMD nanoribbons can be considered as a similar system. They have been generated by laser-induced unzipping of the TMD nanotubes [66] by analogy with the method of manufacturing graphene nanoribbons (GNRs) from carbon nanotubes [67,68] as well as through etching of TMD monolayers [69].

The authors of Ref. [69] claimed that the photoluminescence map of MoS_2 nanoribbons has the peak emission at 1.82 eV. But they did not discuss the physical origin of this peak. This value is close to the experimentally measured exciton energy in MoS_2 monolayer 1.85 eV [70]. Assuming that this peak corresponds to the exciton emission, $E_{1s}^{\rm exc}$, and comparing this value with the known band gap $E_g = 2.15 \pm 0.06$ eV [71], we immediately estimate the the $1s$ exciton binding energy as $E_g - E_{1s}^{\rm exc} = 0.33 \pm 0.06$ eV. This value slightly exceeds the experimentally found value in MoS_2 monolayer 0.31 ± 0.04 eV [72] (although being within the error interval).

To calculate the Bohr radius a_1, we took the experimentally measured effective masses of electrons and holes in MoS_2 monolayer: $m_c^* = 0.67m_0$ and $m_v^* = 0.6m_0$ [73]. The substrate is the SiO_2 plate ($\varepsilon = 3.9$). We obtain $a_1 \approx 0.41$ nm. So, we have a weak dielectric screening case when $a_1 \ll d$. We took the 2D susceptibility of MoS_2 monolayer $\alpha_{2D} = 6.6$ Å [56]. Solving Eq. (30) for a, we find the value of the variation parameter that minimizes the energy $a_{\rm min} \approx 1$ nm, and the exciton binding energy is $|E_{1s}| \approx 0.34$ eV, which is in excellent agreement with the above pointed-out value.

TABLE III. Parameters for the nanoribbon systems on the SiO_2 substrate: the nanoribbon width (d), the exciton energy ($E_{1s}^{\rm exc}$), and the exciton binding energy ($|E_{1s}|$).

System	d (nm)	$E_{1s}^{\rm exc}$ (eV)	$\lvert E_{1s}\rvert$ (eV)	Ref.
MoS_2	300 ± 50	1.82	0.33 ± 0.06	[69]
nanoribbons			0.34	This paper
GNRs	0.74	2.1	~1.8	[76–78]
	0.7–1.1	2.2	~1.5	[79]
	1.7	1.6	~0.7	[80]

Another similar system with a similar geometry are GNRs. They are quasi-1D, planar, and one-atom-thick objects. For comparison, we have collected some currently known experimental values of the parameters of the systems with nanoribbons in Table III.

It is also interesting to note that the scaling laws for excitons in GNRs with armchair-type edges was derived about ten years ago [74]. For the Bohr radius ("the exciton size") [75], the reduced mass, and the exciton binding energy, these laws can be written as

$$a_B = Ad^{\xi}, \mu^* = A_t d^{\tau}, |E_{1s}| = A_k d^{\gamma} \varepsilon_{\rm eff}^{-\alpha},$$

where A, A_t, and A_k are coefficients, and ξ, τ, γ, and α are exponents which depend on the type of armchair GNR [in dependence on the number of lines of carbon atoms N along GNR from one to the other edge: $N = 3p, N = 3p + 1$, and $N = 3p + 2$, where p is an integer], $\xi = 0.6$, $\tau = -1.3$, $\gamma = -0.6$, $\alpha = 0.98$ (for $N = 3p$), $\xi = 0.8$, $\tau = -1.2$, $\gamma = -0.73$, $\alpha = 1$ (for $N = 3p + 1$), and $\xi = 0.3$, $\tau = -2$, $\gamma = -0.55$, $\alpha = 1.16$ (for $N = 3p + 2$).

We hope that similar scaling laws will also be useful as estimates of parameter values for TMD nanoribbons.

V. DISCUSSION AND CONCLUSIONS

Let us now discuss the possible methods to manufacture the heterostructures under consideration. We assume that it will be necessary to combine the method of applying masks followed by annealing with inert gas ions (argon is often used) and molecular beam epitaxy (MBE). We describe possible technological steps in the Supplemental Material [34]. Annealing is necessary for "cutting out" the necessary elements on the TMD monolayer, and MBE is for "overgrowing" of the areas subjected to annealing. Recently, monolayers of $MoSe_2$, WSe_2, $HfSe_2$, and $MoTe_2$ were grown with the help of MBE [35,81–83]. The mask technique was demonstrated by the example of the synthesis of planar heterostructures based on graphene and hexagonal boron nitride [84]. Thus, we believe that it would be possible to manufacture the proposed and here considered theoretically planar $MoTe_2/WTe_2/MoTe_2$ QW.

To conclude, the problem of the size quantization of the charge carrier energy levels in such a QW is solved both in the two-band and in the four-band approximations, although the latter was actually reduced to a single-band approximation, but taking into account the nearest bands. In particular, the initial effective masses in the conduction band m_{ci}^* and in the valence band m_{vi}^* for the QW regions ($i = 1, 2, 3$) are considered to be not equal and are taken from density-functional theory calculations. We calculated the effective masses of electrons and holes in the vicinity of the extremes of the dispersion curves corresponding to the size quantization levels.

Using the results for the effective masses, we considered the excitons in the planar QW based on TMDs monolayers. We proved that there are two regimes of exciton formation, with the weak and strong dielectric screening of the Coulomb potential by the environment.

The former regime is characterized by the quasi-2D behavior of excitons in the ground state and for the first few excited states. Highly excited states in this case fall into the intermediate region between quasi-2D and quasi-1D behavior. The binding energy is calculated using the variational approach. The 2D hydrogen atom eigenfunctions are chosen as the trial wave functions. The latter regime is characterized by the quasi-1D exciton behavior.

The exciton binding energy in the 1D case has a logarithmic divergence. To avoid this divergence, we used a modified Coulomb potential, taking into account the finite QW width. The energy of the ground state of the exciton was calculated variationally. The energy spectrum of the excited states coincides with that of the 3D exciton.

The degeneracy is removed by the angular momentum l in the quasi-2D regime, and the splitting off of the levels occurs down the energy with increasing l. This splitting decreases when the principal quantum number increase.

Let us show how results obtained in this paper can influence the collective properties of excitons in TMD monolayers and heterostructures based on them. Of course, there are many potential consequences; we will discuss only two most obvious of them.

First, we note that the sound velocity in the two-component dilute exciton Bose gas is always larger than in any one-component exciton system in the Bogoliubov approximation as it was shown in Ref. [9]. Two components of excitons are their A and B types. Due to this fact, the critical temperature T_c for superfluidity for the two-component exciton system in a TMD bilayer is significantly higher than T_c in any one-component exciton system. In our system, the existence of a multicomponent Bose gas of weakly interacting excitons is possible. This multicomponent nature can be ensured due to the fact that several size quantization levels of electrons and holes can be populated at once. Electrons and holes at these levels then bind to excitons, which will have different binding energies due to different effective masses of electrons and holes. This observation can also contribute to the occurrence of superfluidity in systems with two parallel QWs considered here, separated by a dielectric layer (the dielectric substrate itself may be such a layer).

Second, placing the system in an open microcavity can provide a rather interesting aspect of the Berezinskii-Kosterlitz-Thouless (BKT) phase transition in polaritons. Namely, the dependence of the BKT critical temperature on detuning between the exciton and photon eigenenergies. The BKT critical temperature can depend nonmonotonically on the detuning [85].

Finally, we will now discuss some prospects for the heterostructures proposed here in the field of applications. Along

with graphene nanoelectronics [86], planar heterostructures of monomolecular thickness based on TMDs could find applications in creating transistors and memory cells, improving integrated circuits, developing thermoelectric devices and fast charges sensors by analogy with the applications of GNRs [87–92].

At the moment, van der Waals heterostructures consisting of atomically smooth sheets of layered semiconductors, such as TMDs, are perfect candidates for engineering next-generation optoelectronic devices. In particular, heterostructures with two to three TMD layers can collect almost 100% of the incident light. The TMD heterostructure may be a type-II heterostructure with an indirect energy gap in the coordinate space (e.g., electrons are located in MoS_2, and holes in WS_2). Nevertheless, in our opinion, planar heterostructures have great potential for use in such devices, having a flat structure.

ACKNOWLEDGMENTS

The author is grateful to S.G. Tikhodeev for the helpful discussion and valuable advice on this publication. The work was supported by the Foundation for the Advancement of Theoretical Physics and Mathematics "BASIS" (the general formulation of the problem) and by the Russian Science Foundation (Project No. 16-12-10538-П, the calculation of the energy spectra of excitons, Sec. IV).

[1] A. K. Geim and I. V. Grigorieva, Nature **499**, 419 (2013).
[2] Yu. E. Lozovik and I. V. Yudson, JETP Lett. **22**, 274 (1975).
[3] Yu. E. Lozovik and I. V. Yudson, Solid State Commun. **19**, 391 (1976).
[4] Yu. E. Lozovik and I. V. Yudson, Sov. Phys. JETP **44**, 389 (1976).
[5] Yu. E. Lozovik and O. L. Berman, JETP Lett. **64**, 573 (1996).
[6] Yu. E. Lozovik and O. L. Berman, JETP **84**, 1027 (1997).
[7] Yu. E. Lozovik and A. A. Sokolik, JETP Lett. **87**, 55 (2008).
[8] Yu. E. Lozovik, S. P. Merkulova, and A. A. Sokolik, Phys. Usp. **51**, 727 (2008).
[9] O. L. Berman and R. Y. Kezerashvili, Phys. Rev. B **93**, 245410 (2016).
[10] O. L. Berman and R. Y. Kezerashvili, Phys. Rev. B **96**, 094502 (2017).
[11] M. M. Fogler, L. V. Butov, and K. S. Novoselov, Nat. Commun. **5**, 4555 (2014).
[12] F.-C. Wu, F. Xue, and A. H. MacDonald, Phys. Rev. B **92**, 165121 (2015).
[13] L. V. Keldysh and A. P. Silin, Sov. Phys. JETP **42**, 535 (1975).
[14] E. A. Andryushin, V. S. Babichenko, L. V. Keldysh, T. A. Onishchenko, and A. P. Silin, Sov. Phys. JETP Lett. **24**, 185 (1976).
[15] E. A. Andryushin, L. V. Keldysh, and A. P. Silin, Sov. Phys. JETP **46**, 616 (1977).
[16] A. P. Silin, Sov. Phys. Solid State **20**, 1983 (1978).
[17] E. A. Andryushin, L. V. Keldysh, V. A. Sanina, and A. P. Silin, Sov. Phys. JETP **52**, 761 (1980).
[18] E. V. Calman, L. H. Fowler-Gerace, D. J. Choksy, L. V. Butov, D. E. Nikonov, I. A. Young, S. Hu, A. Mishchenko, and A. K. Geim, Nano Lett. **20**, 1869 (2020).
[19] R. G. Dickinson and L. Pauling, J. Am. Chem. Soc. **45**, 1466 (1923).
[20] S. Manzeli, D. Ovchinnikov, D. Pasquier, O. V. Yazyev, and A. Kis, Nat. Rev. Mater. **2**, 17033 (2017).
[21] Y. H. Zhou, X. L. Chen, N. N. Li, R. R. Zhang, X. F. Wang, C. An, Y. Zhou, X. C. Pan, F. Q. Song, B. G. Wang, W. G. Yang, Z. R. Yang, and Y. H. Zhang, AIP Adv. **6**, 075008 (2016).
[22] P. Lu, J.-S. Kim, J. Yang, H. Gao, J. Wu, D. Shao, B. Li, D. Zhou, J. Sun, D. Akinwande, D. Xing, and J.-F. Lin, Phys. Rev. B **94**, 224512 (2016).
[23] L. A. Chernozatonskii and A. A. Artyukh, Phys. Usp. **61**, 2 (2018).
[24] J. A. Wilson and A. D. Yoffe, Adv. Phys. **18**, 193 (1969).
[25] K. F. Mak, C. Lee, J. Hone, J. Shan, and T. F. Heinz, Phys. Rev. Lett. **105**, 136805 (2010).
[26] W. Zhao, Z. Ghorannevis, L. Chu, and M. Toh, ACS Nano **7**, 791 (2012).
[27] Y. Zhang, T.-R. Chang, B. Zhou, Y.-T. Cui, H. Yan, Z. Liu, F. Schmitt, L. Lee, R. Moore, Y. Chen, H. Lin, H. T. Jeng, S. K. Mo, Z. Hussain, A. Bansil, and Z. X. Shen, Nat. Nanotechnol. **9**, 6 (2014).
[28] T. Li and G. Galli, J. Phys. Chem. C **111**, 16192 (2007).
[29] S. Lebegue and O. Eriksson, Phys. Rev. B **79**, 115409 (2009).
[30] D. Xiao, G.-B. Liu, W. Feng, X. Xu, and W. Yao, Phys. Rev. Lett. **108**, 196802 (2012).
[31] T. Cao, G. Wang, W. Han, H. Ye, C. Zhu, J. Shi, Q. Niu, P. Tan, E. Wang, B. Liu, and J. Feng, Nat. Commun. **3**, 887 (2012).
[32] H. Zeng, J. Dai, W. Yao, D. Xiao, and X. Cui, Nat. Nanotechnol. **7**, 490 (2012).
[33] K. F. Mak, K. He, J. Shan, and T. F. Heinz, Nat. Nanotechnol. **7**, 494 (2012).
[34] See Supplemental Material at https://link.aps.org/supplemental/10.1103/PhysRevB.102.085303 for the schematic description of the manufacturing process of such heterostructures using the planar heterostructure $MoTe_2/WTe_2/MoTe_2$ growth as an example.
[35] H. J. Liu, L. Jiao, L. Xie, F. Yang, J. L. Chen, W. K. Ho, C. L. Gao, J. F. Jia, X. D. Cui, and M. H. Xie, 2D Mater. **2**, 034004 (2015).
[36] This is a corrected value, because the authors of Ref. [93] have used a clearly underestimated value $E_g = 1.58$ eV. For comparison, the exciton energy in $MoSe_2$ is equal to $E_{1s}^{\mathrm{exc}} = 1.659$ eV [94]. The authors of Ref. [93] experimentally measured the difference between the edges of the valence bands of AlN and $MoSe_2$ (it is equal to 2.84 eV). To obtain the correct value of χ, we took the value $E_g = 2.25$ eV.
[37] A. Kumar and P. K. Ahluwalia, Eur. Phys. J. B **85**, 186 (2012).
[38] C. Gong, H. Zhang, W. Wang, L. Colombo, R. M. Wallace, and K. Cho, Appl. Phys. Lett. **103**, 053513 (2013).
[39] J. Yang, T. Lü, Y. W. Myint, J. Pei, D. Macdonald, J.-C. Zheng, and Y. Lu, ACS Nano **9**, 6603 (2015).

[40] F. A. Rasmussen and K. S. Thygesen, J. Phys. Chem. C **119**, 13169 (2015).

[41] M. V. Durnev and M. M. Glazov, Phys. Usp. **61**, 825 (2018).

[42] A. Kormányos, V. Zólyomi, N. D. Drummond, P. Rakyta, G. Burkard, and V. I. Fal'ko, Phys. Rev. B **88**, 045416 (2013).

[43] The last term is written in such a form as to maintain the origin of the energy $E = 0$ at the middle of the band gap between the lower conduction band and the upper valence band, as shown in Fig. 2(a).

[44] Z. Y. Zhu, Y. C. Cheng, and U. Schwingenschlögl, Phys. Rev. B **84**, 153402 (2011).

[45] N. Zibouche, A. Kuc, J. Musfeldt, and T. Heine, Ann. Phys. **526**, 395 (2014).

[46] A. P. Silin and S. V. Shubenkov, Phys. Solid State **40**, 1223 (1998).

[47] P. V. Ratnikov and A. P. Silin, JETP **114**, 512 (2012).

[48] G. Wang, L. Bouet, M. M. Glazov, T. Amand, E. L. Ivchenko, E. Palleau, X. Marie, and B. Urbaszek, 2D Mater. **2**, 034002 (2015).

[49] D. J. BenDaniel and C. B. Duke, Phys. Rev. **152**, 683 (1966).

[50] G. Bastard, Phys. Rev. B **24**, 5693 (1981).

[51] G. Bastard, Phys. Rev. B **25**, 7584 (1982).

[52] L. D. Landau and E. M. Lifshitz, *Quantum Mechanics, Non-relativistic Theory*, 3rd ed., Course of Theoretical Physics (Pergamon Press, Oxford, 1991), Vol. 3.

[53] M. Farmanbar and G. Brocks, Adv. Electron. Mater. **2**, 1500405 (2016).

[54] Yu. E. Lozovik and I. V. Yudson, Phys. Lett. A **56**, 393 (1976).

[55] L. V. Keldysh, JETP Lett. **29**, 658 (1979).

[56] T. C. Berkelbach, M. S. Hybertsen, and D. R. Reichman, Phys. Rev. B **88**, 045318 (2013).

[57] D. G. W. Parfitt and M. E. Portnoi, J. Math. Phys. **43**, 4681 (2002).

[58] G. Arfken, *Mathematical Methods for Physicists*, 3rd ed. (Academic, London, 1985).

[59] Z. Ye, T. Cao, K. O'Brien, H. Zhu, X. Yin, Y. Wang, S. G. Louie, and X. Zhang, Nature **513**, 214 (2014).

[60] A. A. Al-Hilli and B. L. Evans, J. Cryst. Growth **15**, 93 (1972).

[61] A. Kumar and P. K. Ahluwalia, Physica B **407**, 4627 (2012).

[62] A. Chernikov, T. C. Berkelbach, H. M. Hill, A. Rigosi, Y. Li, O. B. Aslan, D. R. Reichman, M. S. Hybertsen, and T. F. Heinz, Phys. Rev. Lett. **113**, 076802 (2014).

[63] V. S. Babichenko, L. V. Keldysh, and A. P. Silin, Sov. Phys. Solid State **22**, 723 (1980).

[64] R. Loudon, Am. J. Phys. **27**, 649 (1959).

[65] J. Robertson, Eur. Phys. J. Appl. Phys. **28**, 265 (2004).

[66] K. Vasu, S. S. R. K. C. Yamijala, A. Zak, K. Gopalakrishnan, S. K. Pati, and C. N. R. Rao, Small **11**, 3916 (2015).

[67] A. L. Elías, A. R. Botello-Méndez, D. Meneses-Rodríguez, V. J. González, D. Ramírez-González, L. Ci, E. Muñoz-Sandoval, P. M. Ajayan, H. Terrones, and M. Terrones, Nano Lett. **10**, 366 (2010).

[68] P. Sorokin and L. Chernozatonskii, Phys. Usp. **56**, 105 (2013).

[69] Z. Wang, X. Zhang, J. A. Hachtel, A. Apte, C. S. Tiwary, R. Vajtai, J. C. Idrobo, R. Ozturk, and P. Ajayan, Nanoscale Horiz. **4**, 689 (2019).

[70] A. Splendiani, L. Sun, Y. Zhang, T. Li, J. Kim, C.-Y. Chim, G. Galli, and F. Wang, Nano Lett. **10**, 1271 (2010).

[71] C. Zhang, A. Johnson, C.-L. Hsu, L.-J. Li, and C.-K. Shih, Nano Lett. **14**, 2443 (2014).

[72] A. F. Rigosi, H. M. Hill, K. T. Rim, G. W. Flynn, and T. F. Heinz, Phys. Rev. B **94**, 075440 (2016).

[73] T. Eknapakul, P. D. C. King, M. Asakawa, P. Buaphet, R.-H. He, S.-K. Mo, H. Takagi, K. M. Shen, F. Baumberger, T. Sasagawa, S. Jungthawan, and W. Meevasana, Nano Lett. **14**, 1312 (2014).

[74] X. Zhu and H. Su, J. Phys. Chem. A **115**, 11998 (2011).

[75] We note that the Bohr radius of excitons must also depend on the dielectric constant of the environment. We believe, however, that for relatively small values of this constant, one can use the simple scaling law presented in Ref. [74].

[76] S. Linden, D. Zhong, A. Timmer, N. Aghdassi, J. H. Franke, H. Zhang, X. Feng, K. Müllen, H. Fuchs, L. Chi, and H. Zacharias, Phys. Rev. Lett. **108**, 216801 (2012).

[77] R. Denk, M. Hohage, P. Zeppenfeld, J. Cai, C. A. Pignedoli, H. Söde, R. Fasel, X. Feng, K. Müllen, S. Wang, D. Prezzi, A. Ferretti, A. Ruini, E. Molinari, and P. Ruffieux, Nat. Commun. **5**, 4253 (2014).

[78] B. V. Senkovskiy, M. Pfeiffer, S. K. Alavi, A. Bliesener, J. Zhu, S. Michel, A. V. Fedorov, R. German, D. Hertel, D. Haberer, L. Petaccia, F. R. Fischer, K. Meerholz, P. H. M. van Loosdrecht, K. Lindfors, and A. Grüneis, Nano Lett. **17**, 4029 (2017).

[79] G. Soavi, S. D. Conte, C. Manzoni, D. Viola, A. Narita, Y. Hu, X. Feng, U. Hohenester, E. Molinari, D. Prezzi, K. Müllen, and G. Cerullo, Nat. Commun. **7**, 11010 (2016).

[80] A. Tries, S. Osella, P. Zhang, F. Xu, C. Ramanan, M. Kläui, Y. Mai, D. Beljonne, and H. I. Wang, Nano Lett. **20**, 2993 (2020).

[81] L. Jiao, H. J. Liu, J. L. Chen, Y. Yi, W. G. Chen, Y. Cai, J. N. Wang, X. Q. Dai, N. Wang, W. K. Ho, and M. H. Xie, New J. Phys. **17**, 053023 (2015).

[82] R. Yue, A. T. Barton, H. Zhu, A. Azcatl, L. F. Pena, J. Wang, X. Peng, N. Lu, L. Cheng, R. Addou, S. McDonnell, L. Colombo, J. W. P. Hsu, J. Kim, M. J. Kim, R. M. Wallace, and C. L. Hinkle, ACS Nano **9**, 474 (2015).

[83] A. Roy, H. C. P. Movva, B. Satpati, K. Kim, R. Dey, A. Rai, T. Pramanik, S. Guchhait, E. Tutuc, and S. K. Banerjee, ACS Appl. Mater. Interfaces **8**, 7396 (2016).

[84] Z. Liu, L. Ma, G. Shi, W. Zhou, Y. Gong, S. Lei, X. Yang, J. Zhang, J. Yu, K. P. Hackenberg, A. Babakhani, J.-C. Idrobo, R. Vajtai, J. Lou, and P. M. Ajayan, Nat. Nanotechnol. **8**, 119 (2013).

[85] M. N. Brunetti, Optical and Collective Properties of Excitons in 2D Semiconductors, Ph.D. thesis, The City University of New York (2019).

[86] P. V. Ratnikov and A. P. Silin, Phys. Usp. **61**, 1139 (2018).

[87] X. Wang, Y. Ouyang, X. Li, H. Wang, J. Guo, and H. Dai, Phys. Rev. Lett. **100**, 206803 (2008).

[88] W. S. Hwang, P. Zhao, K. Tahy, L. O. Nyakiti, V. D. Wheeler, R. L. Myers-Ward, C. R. Eddy, Jr., D. K. Gaskill, J. A. Robinson, W. Haensch, H. G. Xing, A. Seabaugh, and D. Jena, APL Mater. **3**, 011101 (2015).

[89] E. U. Stützel, M. Burghard, K. Kern, F. Traversi, F. Nichele, and R. Sordan, Small **6**, 2822 (2010).

[90] L. Yu, Y.-H. Lee, X. Ling, E. J. G. Santos, Y. C. Shin, Y. Lin, M. Dubey, E. Kaxiras, J. Kong, H. Wang, and T. Palacios, Nano Lett. **14**, 3055 (2014).

[91] H. Sevinçli, C. Sevik, T. Çain, and G. Cuniberti, Sci. Rep. **3**, 1228 (2013).

[92] S. Fringes, C. Volk, C. Norda, B. Terrés, J. Dauber, S. Engels, S. Trellenkamp, and C. Stampfer, Phys. Status Solidi B **248**, 2684 (2011).

[93] E. Xenogiannopoulou, P. Tsipas, K. E. Aretouli, D. Tsoutsou, S. A. Giamini, C. Bazioti, G. P. Dimitrakopulos, P. Komninou, S. Brems, C. Huyghebaert, I. P. Radu, and A. Dimoulas, Nanoscale **7**, 7896 (2015).

[94] J. S. Ross, S. Wu, H. Yu, N. J. Ghimire, A. M. Jones, G. Aivazian, J. Yan, D. G. Mandrus, D. Xiao, W. Yao, and X. Xu, Nat. Commun. **4**, 1474 (2013).